Influence of design and operation parameters on Hall thruster performances

E. Ahedo and D. Escobar
ETSI Aeronáuticos, Universidad Politécnica de Madrid, 28040 Madrid, Spain

(Received 17 September 2003; accepted 19 April 2004)

A stationary, macroscopic model [E. Ahedo, J. Gallardo, and M. Martínez-Sánchez, Phys. Plasmas 10, 3397 (2003)] is used to carry out parametric investigations on the effects of (i) the discharge voltage, (ii) the gas flow rate, (iii) the axial gradient of the magnetic field, and (iv) the chamber length on the Hall thruster performances and the axial structure of the plasma discharge. The high-thrust and high-specific-impulse modes for dual-mode thrusters are compared too. The results of the simulations agree well with the main tendencies observed in different experiments. The interaction among the several physical phenomena is discussed and useful scaling laws are proposed. Special attention is paid to understand (i) the adjustment of the magnetic field strength with the discharge voltage for optimum operation, (ii) the effect of the magnetic field shape, (iii) the dimensions of the different regions of the discharge, and (iv) the parameter trends needed to increment the propulsive and ionization efficiencies (the product of which determines the thrust efficiency). © *2004 American Institute of Physics.* [DOI: 10.1063/1.1759790]

I. INTRODUCTION

Hall effect thrusters have flown on board USSR satellites since 1972.[1] With the fall of the USSR, the Western countries discovered the maturity of Soviet technology and its excellent suitability for secondary propulsion tasks on geostationary (GEO) satellites, and started to launch ambitious programs of research and development on Hall thrusters.[3–5,7] A significant part of this research has been directed to improve the knowledge of the physical processes and main parameters governing the thruster response. Although a fairly good understanding exists at present on its principles of operation,[8–10] there are still important uncertainties regarding both some plasma phenomena (such as the plasma interaction with the chamber walls, the anomalous electron mobility, and the stability of the discharge) and the influence of the different geometrical and operational parameters on the thruster performance. A consequence of these uncertainties is that most current prototypes still follow closely the basic design characteristics established by the flight-proven USSR thrusters.

Experimental tests have increased extraordinarily over the last decade and are providing very useful data.[11–14,16,17,19–24,26] However, it can be extremely difficult to obtain accurate and detailed measurements of some plasma magnitudes. Furthermore, the complexity of the phenomena involved and the technical constraints explain that the observed operational trends differ sometimes from one experiment to another. Therefore, theoretical and simulation efforts, as the one aimed with this paper, are needed to complement that empirical knowledge.

The work we present here is based on the model of the axial discharge on a Hall thruster presented in Ref. 27, which was shown to give reasonable results for thrusters with long, ceramic chambers [generally known as Stationary Plasma Thruster (SPT)-type thrusters]. The model is stationary, macroscopic, and operates with radially averaged plasma magnitudes. Compared to time-dependent, two-dimensional, particle-based models,[28–30] the characteristics of our model make it fast to run and very suitable for systematic studies on the effects on the thruster response of the different design and operation parameters. In particular, in this paper we analyze in detail the influence of four central parameters of the discharge: the applied discharge voltage, the anode gas flow rate, the axial gradient of the (radial) magnetic field, and the axial length of the chamber. For each parameter, both parametric curves and axial profiles for disparate values of the parameter are presented. Whenever it is possible, the main trends of our simulations are compared with those most commonly observed in experiments. When the numerical and experimental behaviors agree, the main phenomena governing the observed response can be identified and, in some cases, parametric scaling laws can be proposed. When the two trends disagree, we can presume that the dominant physical process is lacking or implemented imperfectly in the model.

Since this paper is, in fact, an application of the work of Ref. 27, the reader is referred to that paper (and a previous one[31]) for the complete description of the principles of operation of a Hall thruster, the theoretical and numerical aspects of the model, and the comparison with related models. Here, Sec. II includes only a very succinct information of the model and the definition of the main variables used throughout the paper. Then, Secs. III–VI treat the influence of each of the four parameters enumerated above. Conclusions are given in Sec. VII. First parametric studies were presented in Ref. 32 and partial results of this work were presented in Refs. 33 and 34.

Section IV includes a section dedicated to the operation at constant electric power. This study is of interest to dual-mode Hall thrusters, which are receiving high attention in new designs for near-future applications.[3] Dual-mode thrusters are needed to carry out satisfactorily, at a nominal electric power, two disparate missions on GEO satellites: orbit top-

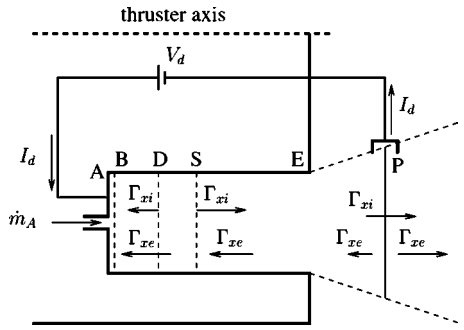

FIG. 1. Sketch of the discharge model. The anode is at point A (with $x_A=0$); the thruster exhaust at point E, and the cathode neutralization surface at point P, points D and S correspond to zero and sonic velocities of the ion flow, and are part of the solution. Point B is the anode-sheath transition. Regions AB, BD, DS, SP correspond to electron-repelling sheath, ion-backstreaming region, main ionization layer, and acceleration region. $\Gamma_{x\alpha}=An_\alpha v_{x\alpha}$, $\alpha=i,e,\ldots$ are axial flows of particles of each of the plasma species.

ping and stationkeeping, which require high thrust F and high specific impulse I_{sp}, respectively. Variable thrust operation has been proposed for drag compensation on low earth orbit (LEO) satellites too.[35]

II. OVERVIEW OF THE MODEL

A. Formulation

The model of the plasma discharge we are going to apply here is described in detail in Refs. 27 and 31; a sketch is shown in Fig. 1. The model consists basically of Eqs. (1)–(8) of Ref. 27; we omit to redefine here all the variables and parameters it needs. (There is only a minor change in the model we used here: In order to include the plasma losses to the front walls of the thruster, the terms accounting for particle and energy losses to the thruster walls have been extended to the near plume. The conclusion over this modification are that the energy losses to the external walls are marginal with respect to the total wall-energy losses, but are important to set the point where T_e becomes maximum.)

Each stationary solution of the plasma equations corresponds to a given set of parameters related to the thruster geometry, the wall material, the magnetic field topology, the operational conditions, and the semiempirical models of certain phenomena. The list of such parameters is the following.

(1) The constants defining the ionization and collisional properties of the propellant (xenon, in the cases treated here).

(2) The chamber dimensions: length L_c, width h_c, and cross-section area A_c.

(3) The axial distance of the virtual neutralizer to the chamber exhaust, L_{cat}.

(4) The shape of the magnetic field profile. We take $\mathbf{B}(x)=B_r(x)1_r$, and $B_r(x)$ is approximated by two semi-Gaussian curves of the form

$$B_r(x)=B_{\max}\exp\left[-\frac{(x-x_M)^2}{L_b^2}\right], \tag{1}$$

with $B_{\max}$ the (maximum) strength of the magnetic field, $L_b=L_{b1}$ for $x<x_M$ and $L_b=L_{b2}$ and for $x>x_M$. Point M is generally placed around the chamber exit.

(5) The discharge voltage V_d.

(6) The flow rate and average axial velocity of the gas injected at the anode, $\dot{m}_A$ and v_{xnA}, respectively.

(7) The cross-over temperature T_1 of the electron fluid for a 100% secondary electron emission yield from the lateral ceramic walls, δ_w. That temperature depends on the wall emission properties and the electron distribution function.[36] Equation (A12) of Ref. 27 [based on Eqs. (12) and (32) of Ref. 37] will be used for $\delta_w(T_e,T_1)$.

(8) The temperature of the electrons emitted by the cathode T_{eP}.

(9) The turbulent diffusion parameter α_{ano} defined in Eq. (A23) of Ref. 27, which measures the relative level of correlated electric fluctuations.

(10) The particle recombination factor at the lateral walls $\tilde{\nu}_w$ defined in Eq. (A6) of Ref. 27.

(11) The accommodation factor for the axial velocity of the neutrals recombined at the walls a_w defined in Eq. (13) of Ref. 27.

The integration scheme of the plasma equations does not use all these parameters as input ones. As a consequence we must proceed numerically in two stages. First, an approximate solution is obtained for the set of input parameters required by the integration algorithm. Then, iterative continuation methods (on eight implicit conditions) are used to adjust the solution to the desired values of the above list of parameters.

As previous works, this one considers only stationary solutions of the *normal operation class* described by Russian authors.[8,9,38] The axial structure of the plasma discharge for this class of solutions consists of an electron-repelling anode sheath, an ion-backstreaming region, the main ionization layer, and internal and external acceleration regions. These are regions AB, BD, DS, DE and EP, respectively, of Fig. 1, limited by distinguished points A (the anode), B (the sheath transition, characterized by a backward ion sonic flux), D (the ion zero-velocity point), S (the forward ion sonic flux point), E (the chamber exit), and P (the virtual neutralizer/cathode). Solutions without an electron-repelling sheath exist but, according to Ref. 9, they have larger heat depositions at the anode and can result in the discharge easily becoming extinguished.

Reference 27 found that the stationary model reproduces the normal operation class only within the narrow parametric range

$$0.514\times10^{-2}<-I_{iA}/I_d<11.4\times10^{-2}, \tag{2}$$

with I_{iA} the ion-backstreaming current reaching the anode and I_d the total discharge current. This thin range for the relative ion back current implies a thin interval of possible values of the magnetic strength $B_{\max}$ when the rest of input parameters are fixed. In other words, the *zero-fluctuation* normal operation class exists only within a narrow band of the parametric region $B_{\max}(V_d,\dot{m}_A,L_c,\ldots)$; see, for instance, Fig. 6 of Ref. 31. The thinness of this band justifies to select an intermediate value of $-I_{iA}/I_d$ to obtain a *single* curve $B_{\max}(V_d,\dot{m}_A,L_c,\ldots)$ which represents the *whole* band of the

normal operation class. In the computations here we used the value $-I_{iA}/I_d=3.93\times10^{-2}$ (which corresponds to a sheath potential jump of $\phi_{AB}=2T_{eB}/e$).

Finally, Ref. 27 suggests that the resulting curve for $B_{\max}(V_d,\dot{m}_A,L_c,...)$ corresponds to the optimum operational value of the magnetic strength determined experimentally. The practical experience with Hall thrusters shows that, for optimum operation, it is convenient to adjust the magnetic strength for each operational case and the optimum $B_{\max}$ corresponds generally to minimum values of the discharge current or the level of current oscillations. Although the present stationary model has no means to confirm it, Ref. 27 argued that the characteristics of the solutions of the normal operation class (such as its axial structure, zero fluctuations, and the behavior of $B_{\max}$ versus V_d) support its suggestion.

B. Partial efficiencies

There is not in the literature a universal definition and nomenclature for the partial efficiencies characterizing the Hall thruster discharge. In addition, some modifications with respect to the nomenclature used in Ref. 27 have been found convenient to do here.

The (thrust) efficiency (based in the anode gas flow rate) is defined as

$$\eta=F^2/2\dot{m}_AP_d,\quad F\simeq\sum_{\alpha=i,n}\dot{m}_{\alpha\infty}v_{x\alpha\infty}, \tag{3}$$

and is simple to measure experimentally. Partial efficiencies of interest are the propellant utilization (or ionization efficiency), $\eta_u=\dot{m}_{i\infty}/\dot{m}_A$, the current utilization, $\eta_{cur}=I_{i\infty}/I_d$, and the voltage utilization, $\eta_{vol}=m_iv_{xi\infty}^2/2eV_d$, ($v_{xi}$, $\dot{m}_i$, and I_i are ion axial velocity, flow, and electrical current, respectively; subscript ∞ refers to downstream conditions, which here are computed at the neutralization surface). The ratio $i_d=\eta_u/\eta_{cur}=m_iI_d/e\dot{m}_A$ is the dimensionless discharge current (or current parameters).

In addition, we define the propulsive efficiency as

$$\eta_{prop}=P_{use}/P_d,\quad P_{use}=\sum_{\alpha=i,n}\dot{m}_{\alpha\infty}v_{x\alpha\infty}^2/2, \tag{4}$$

with P_{use} the useful power. The main contribution to η_{prop} comes from the ion beam and satisfies

$$\dot{m}_{i\infty}v_{xi\infty}^2/2P_d=\eta_{cur}\eta_{vol}. \tag{5}$$

When the ionization is not total, the plasma discharge ejected by the thruster is constituted of two species with different velocities, and η_{prop} and η do not coincide. One has

$$\eta_{prop}-\eta=(1-\eta_u)\times\dot{m}_{i\infty}(v_{xi}-v_{xn})_\infty^2/2P_d. \tag{6}$$

Finally, it is useful to split the power losses as[27]

$$P_{loss}\equiv P_d-P_{use}=P_{ion}+P_{wall}+P_{anode}+P_{plu}, \tag{7}$$

where the four contributions correspond to ionization, heat deposition at the lateral walls and the anode, and losses within the plume region (this last contribution is not totally meaningful since the complete plume is not simulated).

C. Scaling laws

The thickness of the anode sheath L_{AB} is negligible in the chamber scale. Thus, the lengths of the three quasineutral regions of the discharge satisfy

$$L_{BD}+L_{DS}+L_{SP}=L_{AP}. \tag{8}$$

Scaling laws for the lengths of these three regions can be obtained from approximate analyses of the plasma equations in each region.[27,31,39,40]

The acceleration region is characterized by negligible net plasma production, supersonic ion motion, large electric fields, and a voltage drop taking most of the discharge voltage. Thus, approximate equations of the discharge in that region are

$$\begin{aligned}&I_i(x)\simeq\text{const}=I_{iP},\\&-v_{xe}=v_{xi}(I_d-I_{iP})/I_{iP},\\&ed\phi/dx=m_ev_{xe}\omega_e^2/\nu_e,\\&-ed\phi/dx=m_iv_{xi}dv_{xi}/dx.\end{aligned} \tag{9}$$

Operating with these equations and integrating for v_{xi}, one has

$$v_{xiP}-v_{xiS}=(I_d/I_{iP}-1)\int_S^P\overline{\nu}_d dx, \tag{10}$$

where $\overline{\nu}_d=m_e\omega_e^2/\nu_em_i$ represents the (normalized) axial diffusion frequency for electrons. When turbulent diffusion dominates over the rest of collisional effects, one has $\overline{\nu}_d\propto B(x)$. Substituting v_{xi} in terms of ϕ and imposing that the voltage drop across the acceleration region is close to V_d, Eq. (10) yields

$$\sqrt{2eV_d/m_i}\simeq(\eta_{cur}^{-1}-1)\{\overline{\nu}_d\}_{SP}L_{SP}, \tag{11}$$

where $\{\}$ means an average value for the respective magnitude in region *SP*. Numerical results corroborate that the relative errors of this scaling law are below a 20%.[33]

The ion-backstreaming region is governed mainly by the electron dynamics, which are driven towards the anode by a large pressure gradient, whereas the electric field is negligible (except at the transition to the anode sheath). Reference 39 demonstrated that in order to determine the transition to the ionization region (and thus the length of the ion-backstreaming region, L_{BD}) small ionization effects must be taken into account. The approximate analytical solution of Ref. 39 for region *BD* is basically applicable to the present model and yields

$$L_{BD}\propto\{T_e^{3/2}\overline{\nu}_d^{-1/2}\nu_i^{-1/2}\}_{BD}, \tag{12}$$

with $\nu_i=n_nR_i(T_e)$ the ionization frequency. In the ion-backstreaming region, T_e is smaller than the ionization potential E_i and the ionization rate depends exponentially on T_e,

$$R_i(T_e)\propto T_e^{1/2}\exp(-E_i/T_e), \tag{13}$$

which makes L_{BD} very sensitive to the electron temperature in the region.

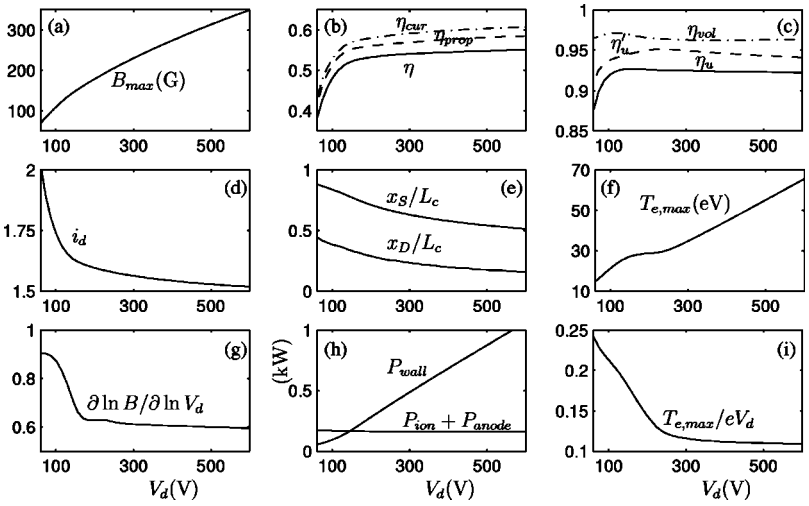

FIG. 2. Evolution of thruster performances with the discharge voltage. Geometrical and operating parameters are $L_c=25$ mm, $A_c=40.06$ mm^2, $h_c=15$ mm, $L_{b1}=15$ mm, $L_{b2}=5$ mm, $x_M=x_E$, $T_1=30$ eV, $\dot{m}_A=4.75$ mg/s. Other parameters of the model are $\alpha_{ano}=9.45\times10^{-3}$, $\tilde{\nu}_w=0.17$, $a_w=0.85$. Plot (*g*) represents the slope of the curve $B_{\max}(V_d)$ of plot (*a*). Plot (i) represents the ratio $T_{e,\max}/eV_d$ of the curve of plot (*f*). In plot (*h*), the ratio P_{anode}/P_{ion} is about 1/4. Partial efficiencies are defined in Sec. II B.

Finally, a simple dimensional analysis of the ionization region suggests that its length satisfies[39]

$$L_{DS}\sim \nu_{iS}^{-1}\sqrt{T_{eS}/m_i}. \tag{14}$$

This law is useful in this form since the temperature at the forward sonic point T_{eS} is found to remain rather invariable (around 20 eV) for all the parametric conditions considered in the paper.

III. INFLUENCE OF THE DISCHARGE VOLTAGE

Figures 2(a)–2(i) show the evolution of the main thruster parameters when the discharge voltage is varied over a large range. Geometrical and operation parameters are listed in the figure caption; they correspond to typical ones for an SPT-100 thruster and were used already in Ref. 27. Figures 3(a)–3(d) compare the axial profiles of the plasma magnitudes for two disparate values of V_d.

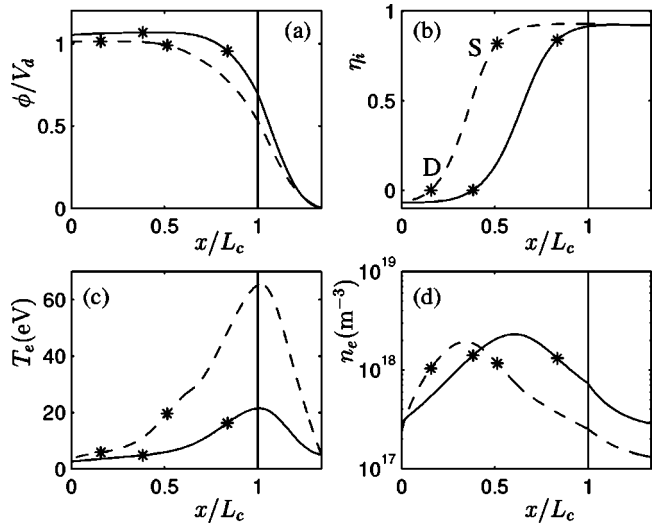

FIG. 3. Axial profiles of the discharge for two particular parametric cases of Fig. 2: $V_d=100$ V (solid lines) and 600 V (dashed lines). In each curve, asterisks represent points *D* (left) and *S* (right). The chamber exit is at the intermediate vertical line, $x/L_c=1$, and the cathode/neutralizer is placed at the right boundary of the plots.

Figure 2(a) shows the adjustment required by the magnetic field strength $B_{\max}$ for optimum operation of the thruster as V_d is changed. The necessity of scaling $B_{\max}$ with V_d is well known experimentally,[8] but there is some controversy on the value of the scaling rate $p=\partial \ln B_{\max}/\partial \ln V_d$ (i.e., the exponent of the potential law $B_{\max}\propto V_d^p$). The value proposed commonly is[8,19] $p\sim0.5$, but other experiments suggest[16,41] $p\sim1$ or even[21] $p\sim1.2$–1.5. Figure 2(g) shows that $p(V_d)$ is not constant with the discharge voltage. For high voltages, p tends to approach 0.5, whereas one has $p\sim1$ for low voltages. The numerical simulations of Ref. 42 for a thruster with metallic walls propose $p\sim1$, and those of Ref. 31 with zero wall losses model yield $p=5/4$. Taking into account that, in our model, energy losses at the walls dominate except for low voltages, Fig. 2(h), the conclusion seems to be that one has $p\sim0.5$ when wall-energy losses are relevant, and $p\sim1$ otherwise.

Figure 2(d) plots the variation of the current parameter $i_d=m_iI_d/e\dot{m}_A$; the discharge current (in amperes) satisfies $I_d\simeq0.731\times i_d\dot{m}_A$, when $\dot{m}_A$ is given in mg/s. The experimental evidence on $I_d(V_d)$ is that: (a) at high voltages, $\partial I_d/\partial V_d$ is weakly positive; (b) at moderate voltages ($V_d\sim200$–400 V, say), $\partial I_d/\partial V_d$ is small, but different experiments show different signs; and (c) at low voltages $I_d(V_d)$ presents a peak and then drops sharply as V_d decreases. At moderate voltages, Refs. 20, 22 (for $BNSiO_2$), and 23 (for the SPT-140) report $\partial I_d/\partial V_d$ negative, Refs. 19, 23 (for the SPT-115), and 24 find positive that derivative, and Refs. 13 and 16 measure an intermediate minimum of I_d in that voltage range. Our simulations yield a small negative slope of $I_d(V_d)$ over the whole voltage interval, which is the consequence of the positive slope for the propulsive efficiency, $\eta_{prop}(V_d)$, Fig. 2(b).

It is known experimentally that the operation at low voltages is highly oscillatory,[20,22] which would explain that our stationary model is unable to recover the sharp decrease of $I_d(V_d)$ at low voltages. In addition, our solutions for very low voltages require to decrease continuously $B_{\max}$, while experiments could have kept $B_{\max}$ too high, which is known to make the discharge unstable.[8,22] A large increase of I_d for

low values of $B_{\max}$, similar to ours at low V_d, is reported in Fig. 4(b) of Ref. 43.

The different partial efficiencies are plotted in Figs. 2(b) and 2(c). A high- and a low-efficiency regimes are observed. The high-efficiency regime corresponds to $V_d > 200$ V, roughly, and thus covers the nominal and high voltage ranges. This is the main regime of operation, when the thruster works at maximum (and almost constant) efficiency, and both thrust F and specific impulse I_{sp} increase as $\propto V_d^{1/2}$. Since the variation of I_d with V_d is weak in this regime, the discharge power $P_d = V_d I_d$ scales practically as $\propto V_d$ and the thrust-to-power ratio follows $F/P_d \propto V_d^{-1/2}$.

Figure 2(h) plots the main contributions to the energy losses P_{loss}, Eq. (7). We observe that $P_{wall} \propto P_d$ whereas $P_{ion}+P_{anode} \sim$ const. In the high-efficiency regime, heat deposition at the lateral walls are the main contribution to P_{loss} and their evolution with V_d makes the propulsive efficiency, η_{prop} [Fig. 2(b)], almost constant. Gas ionization is very efficient in this regime and the propellant utilization, η_u [Fig. 2(c)], is around its maximum value; this value is determined from the balance in the acceleration region between particle recombination at the walls and residual volume ionization.[27] In general, we find that the different efficiencies satisfy

$$\eta_{prop} \simeq \eta_{cur}\eta_{vol} \sim \eta_{cur}, \quad \eta \simeq \eta_u \eta_{prop}. \tag{15}$$

The ratio $\eta/\eta_{prop} \equiv \eta_u'$, an alternative measure of the propellant utilization, is plotted in Fig. 2(c).

Although not shown on Fig. 2, the parametric investigation on V_d was continued up to 800 V. The results suggest that the efficiency $\eta(V_d)$ approaches asymptotically a maximum value (which is the product of the maxima of η_{prop} and η_u). A monotonic evolution of $\eta(V_d)$ is found experimentally in Fig. 7 of Ref. 24, and in some of the curves of Fig. 6 of Ref. 23. However, most experimental data show a peak of the thrust efficiency for a moderate-to-high value of V_d (in the interval 500–800 V typically).[13,16,19,23] This peak could be due to multiple ionization (which is not included in our model) or to phenomena, such as plasma-wall interaction or turbulent diffusion, which are still modeled imperfectly. The presence or lack of local extreme of $\eta(V_d)$ and $I_d(V_d)$ [Fig. 2(d)] at high voltages have likely the same cause.

Thruster performances deteriorate as V_d enters into the low-efficiency regime ($V_d < 200$ V). The efficiency decreases quickly due to the added decrements of η_{prop} and η_u. As V_d is reduced,

(a) $P_{ion}+P_{anode}$ starts to dominate over P_{wall}, Fig. 2(h); since $P_{ion}+P_{anode}$ is almost independent of V_d, the propulsive efficiency decreases.

(b) The maximum plasma temperature $T_{e,\max}$, Fig. 2(f), and the ionization frequency ν_i decrease. This enlarges the effective ionization region and reduces the final propellant utilization, η_u.

The parametric investigation of Fig. 2 was continued down until $V_d \sim 20$ V, to corroborate that no physical limit changing the qualitative behavior of the discharge is reached yet. For a stationary operation at this extremely low voltage, $B_{\max}$ must be reduced to 23.3 G and I_d increases up to 14.1 A. This implies that the current utilization η_{cur} is very low and, although the propellant utilization is still moderate ($\sim$65%), the thrust efficiency drops to a 14%. At $V_d \sim 20$ V, wall losses account only for a 10% of the total energy losses.

Figure 2(e) plots the evolution of the positions of the boundaries D and S of the main ionization region with V_d. That plot is complemented with Fig. 3(b) for the local ion flux fraction,

$$\eta_i(x) = \dot{m}_i(x)/\dot{m}_A; \tag{16}$$

notice that η_i is negative to the left of point D. As V_d increases, ν_i increases and the ionization region becomes shorter. The acceleration region moves slightly upstream and this reduces the axial electric field there, Fig. 3(a); this behavior agrees with the experimental observations of Ref. 24. Figure 3(b) shows that the division of the internal plasma structure on three quasineutral regions and the confinement of the effective ionization layer to region DS is more correct at high voltages. For low voltages, the ionization of the gas extends to the whole discharge chamber (with maximum plasma production in region DS).

Further understanding on the interaction among the different processes and parameters is obtained from the scaling laws proposed in Sec. II. From Eq. (11), $B_{\max}(V_d)$ satisfies

$$B_{\max} \propto \frac{V_d^{1/2}}{L_{SP}} \frac{\eta_{cur}}{1-\eta_{cur}} \sim \frac{V_d^{1/2}}{L_{SP}} \frac{P_{use}}{P_{loss}}. \tag{17}$$

The classical result of $B_{\max} \propto V_d^{1/2}$ is obtained when $L_{SP}(V_d)$ and $\eta_{cur}(V_d)$ are assumed constant.[8] This tends to be true in the high voltage range, because of $P_{loss}/P_d \sim$ const and the small margin of variation of L_{SP}. However, both L_{SP} and η_{cur} decrease as the discharge voltage is reduced. For low enough voltages, Eq. (17) becomes $B_{\max} \propto V_d^{1/2} L_{SP}^{-1} P_{use}$, and the product of the two last factors vary as $\sim V_d^{1/2}$ (or as $\sim V_d^{3/4}$ for zero-wall losses[31]).

As V_d increases, the effective diffusion frequency, $\overline{\nu_d}$ in Eq. (10), increases and this explains the increment of L_{BD} [Eq. (12) and Fig. 2(e)]. The effect of V_d on L_{DS} [Eq. (14) and Fig. 2(e)] is very small and is due to the weak variation of $\{T_e\}_{DS}$ with V_d [Fig. 3(c)].

Figure 2(f) plots the evolution of the maximum plasma temperature $T_{e,\max}(V_d)$. Three different slopes are observed, which correspond to different regimes for the temperature profile: A nonsaturation regime at low V_d ($V_d < 150$ V) with mild temperature gradients and energy losses at the walls; a saturation regime at moderate voltages V_d ($150\text{ V} < V_d < 250$ V), when space-charge saturation of the lateral sheaths near the chamber exit limits $T_{e,\max}$ to T_1 (=30 eV) approximately; and an over-saturation regime at high V_d ($250\text{ V} < V_d$), when ohm heating is strong enough to heat the plasma above the temperature for charge saturation. The profiles of $T_e(x)$ in Fig. 3(c) correspond to the two extreme regimes.

The V_d interval for each of these three regimes depends on the temperature T_1 characterizing the secondary electron emission yield of the walls.[33] Reference 26 reproduces experimentally the two first regimes of our curve $T_{e,\max}(V_d)$. The saturation temperature is higher than ours (50 eV instead of 30 eV), which shifts the saturation regime to larger volt-

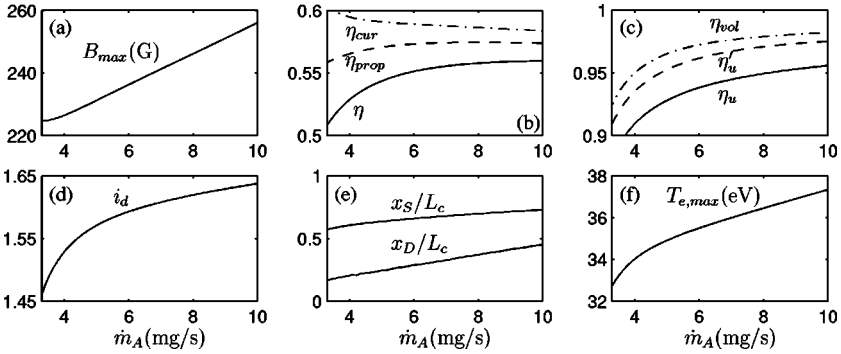

FIG. 4. Evolution of thruster performances with the gas flow rate. The discharge voltage is 300 V and the rest of geometrical and operating parameters are as in Fig. 2.

ages ($V_d > 500$ V) and would explain why the oversaturation regime is not reached in the experiments (which cover only the interval 200–600 V).

The energy balance of the axial discharge is too complex to obtain simple scaling laws for the temperature behavior, so numerical fits for the ratio $T_{e,\max}/eV_d$, Fig. 2(i), are useful. Reference 26 finds $T_{e,\max}/eV_d \sim 0.13$ for the low temperature regime. Our simulations yield $T_{e,\max}/eV_d \sim 0.15-0.20$ for the same regime, and $T_{e,\max}/eV_d \sim 0.11$ for the high temperature regime. The agreement with Ref. 26 is considered very promising if we take into account that several facts suggest that the model for the electron energy balance needs to be improved yet. [On the one hand, Ref. 27 had to introduce a reduction factor to avoid overestimation of particle and energy losses at the lateral walls; on the other hand, in all the plots of $T_e(x)$ shown in this paper the maximum electron temperature tends to be close to the chamber exit, whereas, in many experiments[26,44] this maximum is found inside the chamber, near the end of the ionization layer.]

IV. INFLUENCE OF THE GAS FLOW RATE

This is the second main parameter governing the operation of the thruster. In this section we analyze the effects of modifying it while keeping V_d constant. The main trends observed experimentally are the following. As the gas flow rate is incremented: (a) the magnetic field must be augmented in order to keep a good thruster operation;[19] (b) the propellant utilization and the thrust efficiency increase;[13,19,24] (c) the specific impulse increases slightly;[13,19] and (d) the acceleration layer drifts downstream.[14,17] As it happens with other parameters, the above tendencies are not universal; for instance, Ref. 16 does not find a monotonic trend for $\eta(\dot{m}_A)$.

Figures 4(a)–4(f) show the evolution of the main discharge parameters with the gas flow rate and Figs. 5(a)–5(d) plot axial profiles for two extreme values of $\dot{m}_A$. The simulation results agree totally with the experimental trends reported in the previous paragraph. Two main conclusions are extracted: (a) the discharge is more efficient at high gas flow rates; and (b) relative changes on the discharge magnitudes are larger at low flow rates.

A more detailed analysis of the discharge response to increments of $\dot{m}_A$ shows the following. First, the neutral density and the ionization frequency increase. This reduces the length of the ionization region [Eq. (14) and Fig. 4(e)], defines more clearly the boundaries of that region [Fig. 5(b)], and increases η_u [Fig. 4(c)]; also, a shorter ionization region implies a larger voltage utilization, η_{vol}. Second, a more efficient ionization implies lower temperatures on the ion-backstreaming region [Fig. 5(c)], which increases its length, L_{BD} [Eq. (12) and Fig. 4(e)]. Third, $L_{BD}+L_{DS}$ increases, which makes the acceleration region shorter [Fig. 4(e)]. Four, the decrease of L_{SP} is the main responsible of the moderate adjustment of $B_{\max}(\dot{m}_A)$, [Eq. (11) and Fig. 4(a)]. Five, a shorter acceleration region leads to lower wall losses and a higher η_{prop} [Fig. 4(b)]. Six, the current utilization and the discharge current follow $\eta_{cur} \simeq \eta_{prop}/\eta_{vol}$ and $i_d = \eta_u/\eta_{cur}$; notice in Fig. 4(b) that the thrust efficiency decreases when the current utilization increases. And seven, Fig. 5(c) shows that the displacement of the ionization region towards the chamber exit leads to steeper profiles of $T_e(x)$.

Finally, stationary solutions become difficult to obtain for low flow rates. Indeed these solutions seem to fail to exist beyond a minimum value of $\dot{m}_A$.[34] Since similar losses of stationary solutions exist with two other parametric continuations, the discussion of this subject is postponed to Sec. VI A.

Operation at constant power

In order to keep $P_d = \text{const}$, the discharge voltage needs to be varied in the opposite direction to the gas flow rate. Whereas the two cases discussed before showed the indi-

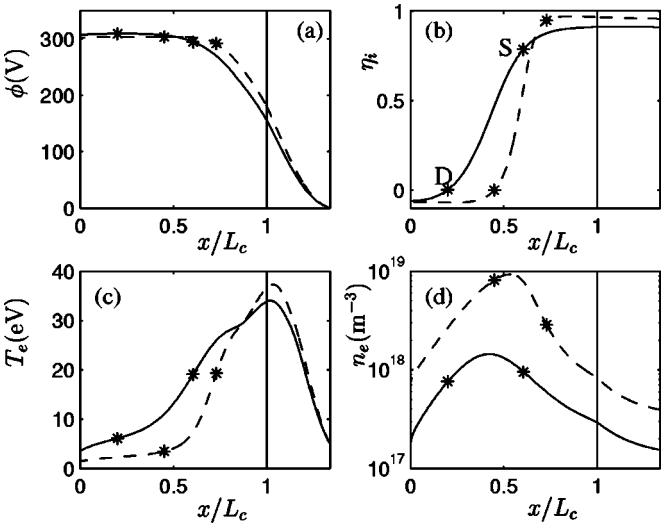

FIG. 5. Axial profiles of the discharge for two particular parametric cases of Fig. 4: $\dot{m}_A = 4$ mg/s (solid lines) and 10 mg/s (dashed lines).

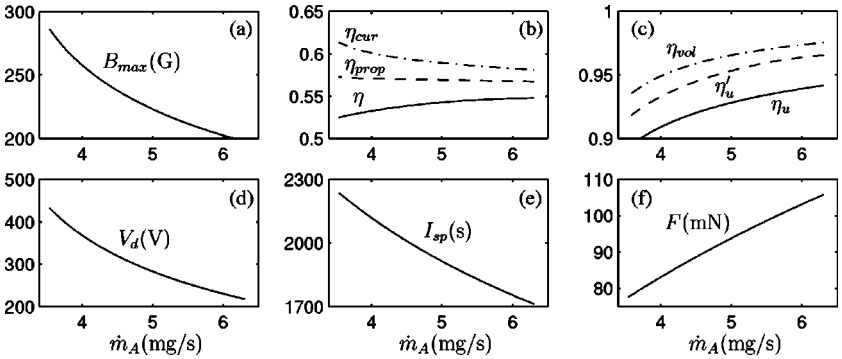

FIG. 6. Evolution of thruster performances with the gas flow rate and discharge voltage, keeping the discharge power constant at 1620 W. Rest of geometrical and operating parameters as in Fig. 2.

vidual effects of V_d and $\dot{m}_A$ on the discharge, the present case allows us to compare the performances of the thruster when this is operated on the high-thrust (low V_d and high $\dot{m}_A$) and the high-I_{sp} (high V_d and low $\dot{m}_A$) modes.

Figures 6(a)–6(f) show the evolution of the main discharge parameters in terms of the variation of $\dot{m}_A$. The corresponding variation of V_d is plotted in Fig. 6(d) and the main output parameters: thrust efficiency, specific impulse, and thrust, are plotted in Figs. 6(b), 6(e), and 5(f). The evolution of the different parameters depends on whether the influence of $\dot{m}_A$ or V_d is dominant. For instance, the adjustment of the magnetic field strength [Fig. 6(a)] is affected mainly by the variation of V_d, in agreement with Ref. 35, whereas η_u and η_{vol} [Fig. 6(c)] depend mainly on the changes of $\dot{m}_A$. The situation is more predictable for other parameters, such as the position of the acceleration region, which is known to move downstream when $\dot{m}_A$ increases of V_d decreases [Figs. 2(e) and 4(e)].

Since heat deposition at the walls dominate the energy losses and scales as $\propto P_d$, the propulsive efficiency [Fig. 6(b)] remains practically constant. From $i_d \simeq \eta_u \eta_{vol}/\eta_{prop}$, it turns out that i_d increases (mildly) with $\dot{m}_A$. The discharge voltage follows $V_d = P_d/i_d \dot{m}_A$ and is proportional to $\dot{m}_A^{-1}$, as a first approximation. The thrust and the specific impulse follow $F = I_{sp}\dot{m}_A \simeq (\eta_u \eta_{prop} \times 2\dot{m}_A P_d)^{1/2}$; thus, one has $F \propto V_d^{-1/2}$ and $I_{sp} \propto V_d^{1/2}$, approximately. The main conclusion of this parametric study is that the thruster operates more efficiently at high mass flows (i.e., on the high-thrust mode) [Fig. 6(b)] which agrees with the experimental observations of Refs. 35 (for $V_d > 200$ V) and 24. In our model the increase of η is due to a higher propellant utilization and not to lower wall energy losses, as suggested by Ref. 35. This explanation would be consistent with the decrease of η observed in this last paper for low discharge voltages ($V_d \sim 100$ V).

V. INFLUENCE OF THE AXIAL GRADIENT OF THE MAGNETIC FIELD

It is universally recognized the importance of shaping correctly the magnetic field for a good performance of a Hall thruster.[9,10,45] The optimization of the magnetic field topology in the discharge chamber is a task of primordial importance in new designs. The magnetic field in the chamber is mainly radial and there is a general accord that a steep axial profile for $B_r(x)$ with the maximum field placed near the chamber exit is desirable. The reasons in favor of it would be:[8–10,45] (a) the magnetic field lines tend to focus the ions away from the walls, thus reducing wall losses; (b) the ion flow is more stable to fluctuations of the electrostatic potential; and (c) the thrust efficiency is found to be higher. This last point is the one we are going to analyze here; notice that the two first ones cannot be studied with the present model. Although point (c) is partially related to point (b), as Ref. 9 suggests, there is direct experimental evidence that the change of the magnetic field gradient modifies the structure of the discharge and, therefore, the thruster performances. In particular, it has been observed that, as the magnetic profiled becomes more pronounced, (a) the acceleration layer moves downstream[14] and (b) the discharge current decreases and the efficiency increases.[14,46] A partial exception to this last observation is provided by Ref. 11, which reports a maximum of efficiency for a rather pronounced magnetic shape.

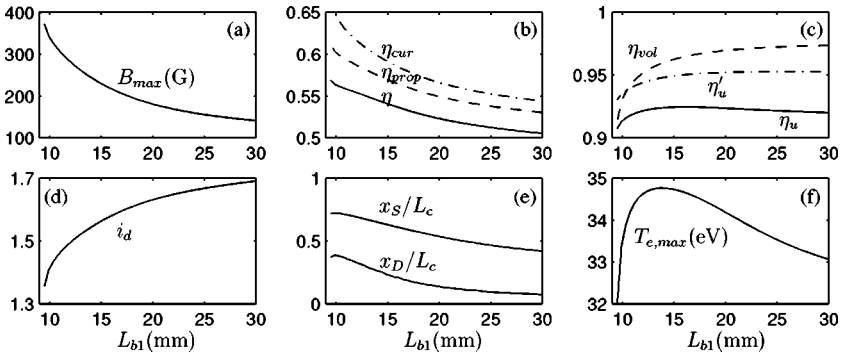

FIG. 7. Evolution of thruster performances with the characteristic internal length of the magnetic field strength, defined in Eq. (1). The discharge voltage is 300 V and the rest of geometrical and operating parameters are as in Fig. 2.

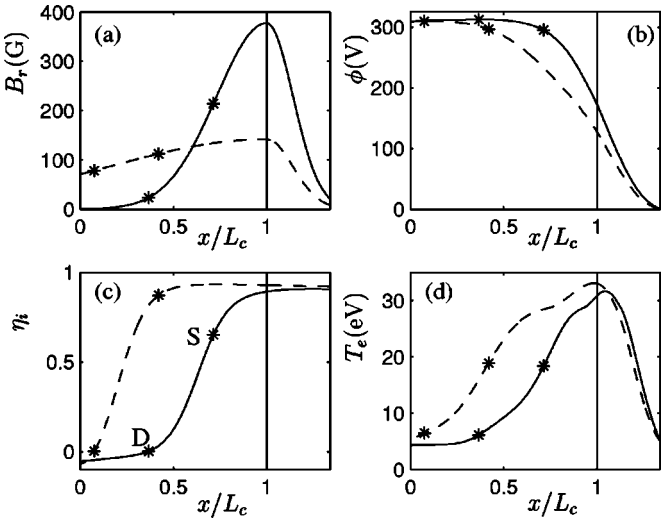

FIG. 8. Axial profiles of the discharge for two particular points of Fig. 7: $L_{b1}=9.49$ mm (solid lines) and 30 mm (dashed lines).

Equation (1) defines the magnetic field shape we used in our simulations. The characteristic axial length of the internal profile is measured by the length L_{b1}. Figures 7(a)–7(f) plot the parametric continuation for L_{b1}; notice that the peak of the magnetic field is fixed at the chamber exit and the external shape is not modified ($L_{b2}=$const). Figures 8(a)–8(d) shows the plasma profiles for two disparate magnetic shapes: in the solid-lines case, the magnetic field is very small near the anode, whereas in the dashed-lines case, it is near uniform along the chamber.

The main features we observe as L_{b1} is increased (and the magnetic field becomes more flat) are the following. First, $B_{\max}(L_{b1})$ [Figs. 7(a) and 8(a)] decreases. The simulations yield $B_{\max}\propto L_{b1}^{-1}$ with a relative error of an 8%. This behavior is justified by the scaling laws (11) and (12) and agrees with the idea that the magnetic integral, $\int B_r(x)dx$, is a relevant parameter on the discharge response.[45] Second, the increase of $B_r(x)$ near the anode reduces the ion-backstreaming region [Figs. 7(e) and 8(c)]; then, since L_{DS} is weakly affected, the acceleration region moves upstream (as the experiments confirm). Third, wall-energy losses increase with L_{SP} and the propulsive efficiency decreases [Fig. 7(b)]. Four, since the propellant utilization is affected weakly by L_{b1},[27] the thrust efficiency decreases too.

Although $T_{e,\max}(L_{b1})$ does not change much [Fig. 7(f)], the temperature profile [Fig. 8(d)] is affected by the position of the acceleration region and the complex energy balance. In particular, observe the small plateaus around the saturation value (30 eV) of the plasma temperature; they are due to the approximate balance between the ohm heating and the wall cooling of the plasma. Similar plateaus are found in the profiles of T_e of the rest of the cases.

No numerical solution is found for a characteristic length below $L_{b1}\simeq 9.5$ mm, the solid-line case of Fig. 8. A turning point on the parametric curves of Fig. 7 is detected there. We tried to continue the parametric curves into a second branch, with L_{b1} increasing again, but the continuation algorithms did not converge.

VI. INFLUENCE OF THE CHAMBER LENGTH

The optimization of the channel length L_c is an important aspect of the Hall thruster design. However, detailed data on the effect of modifying L_c is scarce. In Ref. 12 it is found experimentally that the current utilization and the efficiency decrease as the chamber length is increased. In addition, it is argued (but not verified experimentally) that the propellant utilization η_u must increase with L_c increasing, and it is concluded that the maximum efficiency must be obtained for an intermediate value of the chamber length. The effects of modifying the chamber length are analyzed experimentally in Ref. 13 too. It is found that (for each $\dot{m}_A$) there is an optimum L_c that maximizes the propellant utilization and, as a result, the efficiency.

Figures 9(a)–9(f) depict our parametric results when L_c is modified. In order to separate the influence of L_c from that of the internal shape of the magnetic field, we keep $L_{b1}/L_c=$const; however, external lengths, such as the magnetic gradient length, L_{b2}, and the distance to the neutralizer, L_{cat}, were not scaled with L_c. The axial profiles for cases $L_c=17$ mm and 42.5 mm are plotted in Figs. 10(a)–10(d); the use of a dimensionless abscissa, x/L_c, allows us a more comprehensive comparison of these disparate cases.

The adjustment of $B_{\max}(L_c)$ follows $B_{\max}\propto L_c^{-1}$ (with a relative error of a 3%), due to the same reasons than in the continuation on L_{b1} (notice that L_{b1}/L_c is constant here). For short chambers, the ionization efficiency (and the voltage utilization) increase with L_c [Figs. 9(c) and 10(b)]; for long enough chambers, η_u becomes practically independent of L_c.[27] An interesting (and no obvious) result related to the discharge response is that the acceleration region does not move towards the chamber exhaust, as L_c is reduced; indeed,

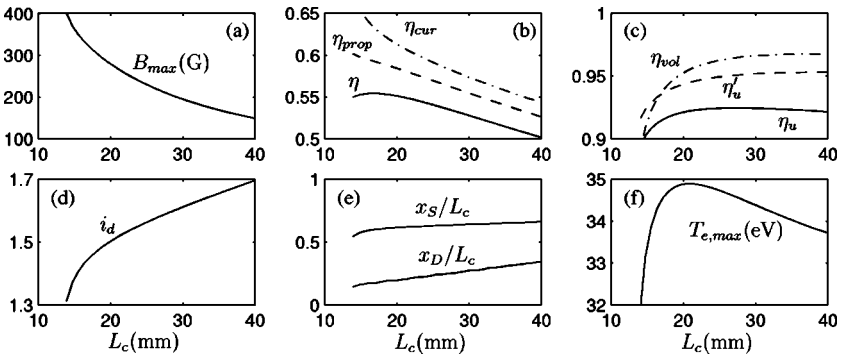

FIG. 9. Evolution of thruster performances with the channel length, keeping the ratio L_{b1}/L_c constant at 0.6. The discharge voltage is 300 V and the rest of geometrical and operating parameters are as in Fig. 2.

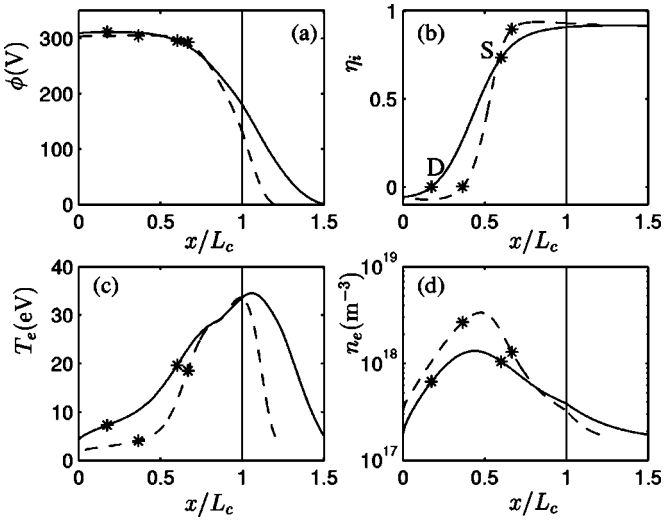

FIG. 10. Axial profiles of the discharge for two particular points of Fig. 9: $L_c=17$ mm (solid lines) and 42.5 mm (dashed lines).

L_{SP}/L_c increases weakly [Fig. 9(e)] and this behavior is justified by Eq. (11). This last fact and the shorter ionization layer explains that L_{BD} takes most of the change of L_c. The increase of L_{SP} with L_c augments the wall-energy losses and reduces the propulsive efficiency [Fig. 9(b)]. Finally, the experimental evidence is confirmed; η is maximum for an intermediate chamber length ($L_c=16.5$ mm in our simulations) and this optimum length comes out from the trade-off between the opposite behaviors of $\eta_{prop}(L_c)$ and $\eta_u(L_c)$.

Loss of stationary solutions

The parametric continuations on L_c stop to yield valid solutions for L_c below 13.7 mm, approximately. Therefore, the four parametric studies we have carried out show that our stationary model do not yield solutions when (i) the mass flow rate is too low, (ii) the magnetic field inside the chamber is too pronounced (i.e., too low in the anode region), and (iii) the chamber length is too short. We are not sure on whether the exact cause of these behaviors is physical or numerical. There are three significant coincidences in the respective limit cases for each parameter: (i) the dimensionless current, i_d, reaches a minimum value of around 1.3, (ii) the ionization is not very efficient and tends to occupy most of the channel, and (iii) the maximum plasma temperature approaches the saturation value. There are relevant differences too, such as (i) the length of the ion-backstreaming region is large for the case of L_{b1}, but it is small in the two other cases, and (ii) the efficiency behaves differently for the three limit cases. The coincidences on a minimum value of i_d and a deficient ionization suggest a physical reason for the loss of solutions. Our solution class (stationary and with a high propellant utilization) becomes increasingly difficult to sustain as i_d approaches one. Thus, the loss of solutions could be related to a sharp transition to another operational regime, either oscillatory or with a low efficiency. (In the first version of the present axial model,[39] which considered neither heat conduction nor lateral wall losses, a stationary, low-efficiency regime was clearly determined, with no continuous transition, apparently, to the high-efficiency regime.) The coincidences on the behavior of $T_{e,\max}$ can be due to either physical or numerical reasons. When $T_{e,\max}$ crosses the saturation value, T_1, the energy balance is strongly modified by the sharp change on the value of P_{wall}.[27] On the numerical side, the continuation routines have difficulties in crossing these parametric regions and could be nonconvergent. On the physical side, it could happen that a stationary energy equilibrium could not be sustained longer. In conclusion, further work is needed to clarify the discharge response around the limit cases of the parametric continuations.

VII. CONCLUSIONS

A recent stationary, macroscopic model of the discharge in a Hall thruster is found to be very suitable to investigate the influence of four central parameters on the discharge response. Many of the principal trends observed experimentally have been reproduced and physically understood. Scaling laws of interest have been proposed and checked.

The main conclusions that have been reached are the following.

(1) The thrust efficiency is mainly the product of the ionization and propulsive efficiencies. The propulsive efficiency measures the relative useful power, is lower than the ionization efficiency, and should be the main focus of design optimization. A high propulsive efficiency is favored by (moderately) large discharge voltages, large magnetic field gradients, and short chamber lengths. A high propellant utilization is favored mainly by high enough mass flows and chamber lengths. In particular, these behaviors explain that there is an optimum length chamber that maximizes the thrust efficiency.

(2) The operation of dual-mode thrusters at constant power has shown a larger efficiency in the high-thrust mode, but differences with the high-I_{sp} mode are not very large, thanks to the opposite trends of the propulsive and ionization efficiencies.

(3) The optimum adjustment law for $B_{\max}\propto V_d^p$ yields $p\sim 0.5$ when wall-energy losses dominate and $p\sim 1$ otherwise. This law comes out mainly from the characteristics of the acceleration region. The adjustment for $B_{\max}(L_c)$ is mainly based on the preservation of the magnetic integral (i.e., the global electron axial diffusion). The adjustment required for $B_{\max}(\dot{m}_A)$ is small.

(4) As a general rule, the position and extension of the three quasineutral regions of the discharge are largely affected by the four parameters we have studied.

(5) Stationary solutions at low discharge voltages require low magnetic fields and very high discharge currents, which penalizes strongly the propulsive efficiency.

(6) Stationary solutions are lost for small mass flows, small chamber lengths, and large magnetic axial gradients. The reasons for it are not totally clear yet. They seem related to difficulties on attaining high ionization and keeping a stationary energy balance.

The good results obtained with these parametric studies confirm the model as a useful tool to carry out quick predesign studies of Hall thruster chambers. This does not exclude (but makes more necessary) to improve its weakest points,

related to phenomena that are not fully understood yet. Reference 27 identifies (i) the role and level of turbulent diffusion and (ii) the effects on the electron distribution function of the interaction with the chamber ceramic walls, as the main aspects requiring further research.

ACKNOWLEDGMENTS

The authors thank the computational aid of F. Parra and C. Pérez. This work received support from the European Office of Aerospace Research and Development, under Contract No. FA8655-02-M4080, and the Ministerio de Ciencia y Tecnología of Spain, under Project No. BFM-2001-2352.

[1] M. Martínez-Sánchez and J. Pollard, J. Propul. Power **14**, 688 (1998).
[2] *Proceedings of 38th Joint Propulsion Conference, Indianapolis, IN*, edited by American Institute of Aeronautics and Astronautics (Washington, DC, 2002).
[3] R. S. Jankovsky, D. T. Jacobson, C. J. Sarmiento, L. R. Piñero, D. H. Manzella, R. R. Hofer, and P. Y. Peterson, paper AIAA 2002-3675 in Ref. 2.
[4] R. Spores and M. Birkan, paper AIAA 2002-3558 in Ref. 2.
[5] S. Tverdokhlebov *et al.*, paper AIAA 2002-3562 in Ref. 2.
[6] *Proceedings of the 28th International Electric Propulsion Conference, Toulouse, France*, edited by Electric Rocket Propulsion Society (Cleveland, OH, 2003).
[7] G. Saccoccia, paper IEPC 03-341 in Ref. 6.
[8] V. Kim, J. Propul. Power **14**, 736 (1998).
[9] V. Zhurin, H. Kaufman, and R. Robinson, Plasma Sources Sci. Technol. **8**, R1 (1999).
[10] A. Morozov and V. Savelyev, *Reviews of Plasma Physics* (Kluwer Academic, New York, 2000) Vol. 21, Chap. 2.
[11] V. Gavryushin, V. Kim, V. Kozlov, K. Kozubsky, G. Popov, A. V. Sorokin, M. Day, and T. Randolph, in *Proceedings of the 30th Joint Propulsion Conference, Indianapolis, IN*, edited by American Institute of Aeronautics and Astronautics (Washington, DC, 1994) paper AIAA 94-2858.
[12] K. Komurasaki, K. Mikami, and D. Kusamoto, in *32nd Joint Propulsion Conference, Lake Buena Vista, FL*, edited by American Institute of Aeronautics and Astronautics (Washington, DC, 1996) paper AIAA 96-3194.
[13] J. Ashkenazy, Y. Raitses, and G. Appelbaum, Phys. Plasmas **5**, 2055 (1998).
[14] Y. Raitses, J. Ashkenazy, and G. Appelbaum in *Proceedings of the 34th Joint Propulsion Conference, Cleveland, OH*, edited by American Institute of Aeronautics and Astronautics (Washington, DC, 1998) paper AIAA 98-3640.
[15] *Proceedings of the 27th International Electric Propulsion Conference, Pasadena, CA, USA*, edited by Electric Rocket Propulsion Society (Cleveland, OH, 2001).
[16] B. Pote and R. Tedrake, paper IEPC-01-035 in Ref. 15.
[17] J. Haas and A. Gallimore, Phys. Plasmas **8**, 652 (2001).
[18] *Proceedings 37th Joint Propulsion Conference, Salt Lake City, UT*, edited by American Institute of Aeronautics and Astronautics (Washington, DC, 2001).
[19] D. Manzella, D. Jacobson, and R. Jankovsky, paper AIAA-2001-3774 in Ref. 18.
[20] L. Mason, R. Jankovsky, and D. Manzella, paper AIAA 2001-3773 in Ref. 18.
[21] R. Hofer and A. Gallimore, paper AIAA 2002-4111 in Ref. 2.
[22] N. Gascon, M. Dudeck, and S. Barral, Phys. Plasmas **10**, 4123 (2003).
[23] A. Bouchoule, A. Lazurenko, V. Vial, V. Kim, V. Kozlov, and A. Skrylnikov, paper IEPC 03-211 in Ref. 6.
[24] R. R. Hofer and R. H. R. Jankovsky, paper IEPC 03-142 in Ref. 6.
[25] *Proceedings of the 39th Joint Propulsion Conference, Huntsville, AL*, edited by American Institute of Aeronautics and Astronautics (Washington, DC, 2003).
[26] Y. Raitses, D. Staack, L. Dorf, and N. Fisch, paper AIAA 2003-5153 in Ref. 25.
[27] E. Ahedo, J. Gallardo, and M. Martínez-Sánchez, Phys. Plasmas **10**, 3397 (2003).
[28] J. M. Fife, Ph.D. thesis, Massachusetts Institute of Technology, 1998.
[29] J. Boeuf and L. Garrigues, J. Appl. Phys. **84**, 3541 (1998).
[30] G. Hagelaar, J. Bareilles, L. Garrigues, and J. Boeuf, J. Appl. Phys. **91**, 5592 (2002).
[31] E. Ahedo, J. Gallardo, and M. Martínez-Sánchez, Phys. Plasmas **9**, 4061 (2002).
[32] E. Ahedo, P. Martínez-Cerezo, and M. Martínez-Sánchez, *SP-465: Third Spacecraft Propulsion Conference, Cannes (Francia)*, edited by European Space Agency (Noordwijk, The Netherlands, 2000) pp. 323–330.
[33] E. Ahedo, J. Gallardo, F. Parra, and C. P. Trigo, paper IEPC-03-331 in Ref. 6.
[34] E. Ahedo, D. Escobar, C. Pérez, and J. Rus, paper AIAA 2003-4707 in Ref. 25.
[35] Y. Raitses, M. Guelman, J. Ashkenazy, and G. Appelbaum, J. Spacecr. Rockets **36**, 875 (1999).
[36] J. Fife, M. Martínez-Sánchez, and J. Szabo, in *Proceedings of the 33rd Joint Propulsion Conference, Seattle, WA*, edited by American Institute of Aeronautics and Astronautics (Washington, DC, 1997) paper AIAA 97-3052.
[37] E. Ahedo, Phys. Plasmas **9**, 4340 (2002).
[38] A. Bishaev and V. Kim, Sov. Phys. Tech. Phys. **23**, 1055 (1978).
[39] E. Ahedo, P. Martínez-Cerezo, and M. Martínez-Sánchez, Phys. Plasmas **8**, 3058 (2001).
[40] A. Cohen-Zur, A. Fruchtman, J. Ashkenazy, and A. Gany, Phys. Plasmas **9**, 4363 (2002).
[41] V. Khayms and M. Martínez-Sánchez, *Progress in Astronautics and Aeronautics*, edited by American Institute of Aeronautics and Astronautics (Washington, DC, 2000) Vol. 187, Chap. 9.
[42] V. Blateau, M. Martínez-Sánchez, O. Batishchev, and J. Szabo, paper IEPC 01-37 in Ref. 15.
[43] A. Morozov, Y. Esipchuk, G. Tilinin, A. Trofimov, Y. Sharov, and G. Y. Shchepkin, Sov. Phys. Tech. Phys. **17**, 38 (1972).
[44] J. Haas and A. Gallimore, in *36th Joint Propulsion Conference, Huntsville, Alabama*, edited by American Institute of Aeronautics and Astronautics (Washington, DC, 2000) paper AIAA 2000-3422.
[45] H. Kaufman, AIAA J. **23**, 78 (1985).
[46] V. Gavryushin and V. Kim, Sov. Phys. Tech. Phys. **26**, 505 (1981).